PHYSICAL REVIEW MATERIALS **6**, 126001 (2022)

Molecular dynamics simulation of structural evolution in crystalline and amorphous CuZr alloys upon ultrafast laser irradiation

Djafar Iabbaden,[1,*] Jonathan Amodeo,[2,3] Claudio Fusco,[2] Florence Garrelie,[1] and Jean-Philippe Colombier[1,†]
[1]*Univ Lyon, UJM-Saint-Etienne, CNRS, IOGS, Laboratoire Hubert Curien UMR5516, F-42023 St-Etienne, France*
[2]*Univ Lyon, INSA Lyon, CNRS, MATEIS, UMR 5510, F-69621 Villeurbanne, France*
[3]*Aix Marseille Univ, Université de Toulon, CNRS, IM2NP Marseille, France*

(Received 14 April 2022; revised 1 July 2022; accepted 14 November 2022; published 7 December 2022)

A promising route for manufacturing emergent metamaterials is the use of ultrafast laser pulses in complex alloy processing. Laser-induced structural transformations in Zr-based alloys for crystalline and glassy states are investigated here. The ultrafast thermomechanical response is compared between relevant stable crystalline structures B_2-$Cu_{50}Zr_{50}$, $C11_b$-$Cu_{33.3}Zr_{66.7}$ and the amorphous structures α-$Cu_{50}Zr_{50}$, α-$Cu_{33.3}Zr_{66.7}$. The subsurface modification resulting from ultrafast laser irradiation is investigated by a hybrid simulation to capture the phenomenon occurring at a picosecond time scale. This combines a two temperature model and molecular dynamics approaches to simulate laser matter interaction at the mesoscale. Our results indicate that the involved structural dynamics strongly depend on the initial atomic composition and phase structure. In particular, a martensite phase transition is unveiled for B_2 crystalline alloy, and defects are induced in the irradiated $C11_b$ phase, whereas the amorphous state of photoexcited metallic glasses remains remarkably preserved.

DOI: 10.1103/PhysRevMaterials.6.126001

I. INTRODUCTION

Upon ultrafast laser structuring process, light is temporally confined allowing photoexcitation of band gap materials and a quasi-isochoric heating of metallic or semimetallic materials [1]. At the same time, beam focusing and polarization manipulation allow the energy concentration at the nanoscale [2] and significant results evidenced that phase transformation can be triggered in material alloys, implying both glasses and crystalline materials [3–6]. Subpicosecond laser irradiation shorter than electron − phonon relaxation time is able to cause structural distortion in solid lattices, inducing order-disorder changes in covalently-bonded materials [7,8], metal-insulator transitions [9,10]. The typical martensitic transformation is the face-centered-cubic to body-centred-cubic transformation in steels [11]. Martensite structural changes occur in shape memory alloys, and also in pure elements such as tantalum, and titanium [12,13], where a body-centred-cubic to hexagonal-close-packed transformation is observed [14]. Besides, femtosecond (fs) irradiation of titanium alloys revealed the opportunity to tune structural states of their surface, through a laser-driven α to β phase transformation related to the combined effect of ultrafast heating and cooling or strong shock waves [15]. Recent theoretical predictions highlighted that direct solid-solid transition can be transiently triggered in pure metals by ultrafast laser due to the strong coupling between electronic and ionic structures but remains to be experimentally confirmed for permanent crystalline states [16,17]. Metallic glasses, usually formed by liquid quenching, have also shown capability for undergoing crystallization during molding on the micrometer (μm) to nanometer (nm) scale owing to the low viscosity in the supercooled liquid state [18]. This behavior remains unexplored in response to ultrashort laser irradiation.

In this paper, we employ atomistic modeling to investigate laser-induced architecturation of CuZr alloys. This reveals how mechanical stress induced by shock wave affects the structural features, and the stability of certain compositions. The energy dynamics of the photoexcited solid is investigated by employing the two-temperature model (TTM) [19]. This approach is used to describe the thermal diffusion and the energy transfer from the excited electrons to the colder lattice under an electron − phonon nonequilibrium state. In order to understand the response to this swift heating, it is necessary to couple the TTM to classic hydrodynamics or molecular dynamics (MD). TTM-MD has successfully been implemented to provide insights on phase transition [[20], [21]], defect formation [22,23], or laser-ablation mechanisms [24]. Most of the reported works using MD approaches explored the interaction of an ultrafast laser with pure metals as Al [25], Cr [26], Cu [27], and Au [28], semiconductors as Si [29] or even graphite [30]. A first attempt to understand the behavior of a CuZr under a ultrafast laser shot was done in [31] but no phase transitions were detected especially in the crystalline states. The choice of a CuZr system is not fortuitous, since in its amorphous state this specific metallic glass (MG) plays a fundamental role in advanced material engineering, from biomedical applications for antimicrobial properties [32] to metallurgy and anticorrosion properties [33]. Recently, this kind of amorphous system was irradiated by ultrafast laser for surface nanostructuring applications [34,35]. Single shot ultrafast laser interaction with metallic alloys has been

---

[*] djafar.iabbaden@univ-st-etienne.fr
[†] jean.philippe.colombier@univ-st-etienne.fr

investigated in nanostructuring conditions far from equilibrium conditions. Unusual phase transformation emerges at the surface or in the subsurface region of the ultrafast-irradiated target. Phase transitions are expected to originate from atomic rearrangements either due to thermoelastic stresses [36–38] in response to the propagation of the pressure wave throughout the system relaxation or during the resolidification process that proceeds under high undercooling conditions [23,39,40]. This paper aims to settle the relative role of both processes by focusing on the CuZr binary alloys with different compositions in both crystal and amorphous structures, in particular for α-Cu$_{50}$Zr$_{50}$ and α-Cu$_{33.3}$Zr$_{66.7}$. Our results demonstrate that phase stability upon laser pulse and microstructural transformations depend on the initial crystallographic structure. The semiempirical potential used to model the vitrification of the Cu-Zr alloys confirms that the initial concentrations (50% and 66.7% of Zr) are stable and leads to a reasonable agreement with the experimental and phase diagram observations [41]. In contrast, thermodynamical response is substantially different for amorphous systems irradiated by similar laser conditions. No structural transformation was observed for the evaluated stoichiometry as MG accommodates the distortion even in the lack of long-range translational order maintaining mechanical stability.

II. COMPUTATIONAL MODELLING

The numerical simulations are carried out using the LAMMPS software [42] in which the CuZr systems are computed using the embedded atom model (EAM) of Mendelev *et al.* [43]. A timestep of $\Delta t = 1$ fs is used throughout the simulations in which the local atomic structures are investigated using the polyhedral template matching algorithm (PTM) [44] as implemented in the OVITO software [45].

A. TTM-MD theoretical framework

The TTM model is executed using the USER-MISC package [46] derived from cascade algorithm simulations [47]. This LAMMPS package accounts for electronic effects and provides the implementation of the TTM-MD hybrid method algorithm as described in [20,21,48–52]. This combines two schemes where electrons are modeled as a continuum on a regular grid, and ions are tracked using a regular classical MD as

$$m_j \frac{\partial v_j}{\partial t} = -\nabla_j U(r_1, \dots, r_n) + F_j^{\text{lang}}(T_e - T_a) - \frac{\nabla P_e}{n_i} \tag{1}$$

where m_j and v_j are respectively the mass and velocity of the jth atom, $\nabla_j U(r_1, \dots, r_n)$ is the force produced by the empirical potential. P_e is the electronic pressure, and n_i is the ionic density. T_a, T_e represent the ionic and electronic temperature respectively. The t, r represent the considered time and position, where the F_j^{lang} is the random force due to the electron-phonon coupling defined as

$$F_j^{\text{lang}}(t) = -\gamma_p m_i v_i + \tilde{F}(t), \tag{2}$$

γ_p represents the electron − phonon contribution coefficient. The $\tilde{F}$(t) is a random force giving the effect of noise satisfying the fluctuation dissipation theorem [53,54],

$$\begin{cases} \langle \tilde{F}(t) \rangle = 0 \\ \langle \tilde{F}(t').\tilde{F}(t) \rangle = 2k_B T_e m_i \gamma_p \delta(t' - t) \end{cases} \tag{3}$$

where k_B is the Boltzmann constant, m_i is the atomic mass of the used species, and $\delta(t' - t)$ is the Dirac function.

The electronic subsystem is modeled by a one dimensional heat diffusion equation in the x direction with an external heat source

$$C_e(T_e)\frac{\partial T_e}{\partial t} = \nabla(\kappa_e(T_e)\nabla T_e) - g_p(T_e - T_a) + \frac{I(t)e^{-x/l_p}}{l_p} \tag{4}$$

where κ_e is the electronic thermal conductivity, $C_e(T_e)$ the electronic specific heat, l_p the penetration depth, g_p electron − phonon coupling strength coefficient, and $I(t) = I_0\ \Pi(\text{t})$ where Π(t) is a rectangular function with $\Pi(t) = 1$ if $0 < t < 100$ fs and 0 otherwise. The I_0 is the initial laser intensity. The equivalent absorbed laser fluence is defined as $F_{\text{abs}} = I.\tau$ with τ the pulse duration. Furthermore, the friction due to the electron-ion coefficient is given by

$$g_p = \frac{3Nk_B\gamma_p}{\Delta V m_i}. \tag{5}$$

ΔV and N represent the volume of a unitary electronic grid and the total number of atoms inside each grid element respectively.

The $C_e(T_e)$ is considered electronic temperature dependent, this quantity is either obtained by using available experimental data (cf. Table I) or by performing first principle calculation (cf. Table S1 in the Supplemental Material [60]) and fit the result according to the following equation:

$$C_e(X) = C_0 + (a_0 + a_1X + a_2X^2 + a_3X^3 + a_4X^4)e^{-(AX)^2} \tag{6}$$

where C_0, a_0, a_1, a_2, a_3, a_4, A are the corresponding fitting parameters and $X = T_e/1000$.

An electron pressure contribution $P_e(T_e) = BC_e(T_e)T_e$ is expected to induce a blast force in the computation according to Eq. (1), with B a material-dependent constant. In the present study, we have neglected this surface effect and fix $B = 0$. For the crystalline structures the $C_e(T_e)$ are computed using density functional theory. However, for the amorphous structures, a free electron model is used as $C_e(T_e) = \gamma T_e$ [55]. The electronic specific heat coefficient γ of each composition, reliable experimental data mentioned in [56,57] are available. The values are summarized in Table I.

The electron − phonon coupling factor g_p is considered as constant in this model. However, a linear response approximation [31] relation is used to compute the electron − phonon coupling factor in both crystalline and amorphous states by the relation $g_p = xg_p^{\text{Cu}} + (1 - x)g_p^{\text{Zr}}$. Where x is the percentage of Cu atoms present in a given Cu$_x$Zr$_{1-x}$ structure.

A proper descriptions of the samples thermodynamics are ruled by $\kappa_e(T_e)$. In fact, to feed the simulation model, experimental data are taken at 300 K. The thermal diffusion is related to the previous quantities by

$$D_e = \frac{\kappa_e(T_e)}{C_e(T_e)}. \tag{7}$$

TABLE I. Physical properties of crystalline and amorphous CuZr binary systems, namely specific heat constant γ and electron − phonon factor g_p, electronic thermal conductivity κ_e, and electronic thermal diffusion D_e.

Property Unit	ρ_0 [$\mathrm{g\,cm^{-3}}$]	g_p [10^{17} $\mathrm{Wm^{-3}K^{-1}}$]	γ [$\mathrm{Jm^{-3}K^{-2}}$]	κ_e [$\mathrm{Wm^{-1}K^{-1}}$]	D_e [10^{-5} $\mathrm{m^2s^{-1}}$]	l_p [nm]
B_2-$Cu_{50}Zr_{50}$	7.66	3.75 [31]	245.13 [31,57]	7.41 [67]	10.07	14.30
$C11_b$-$Cu_{33.3}Zr_{66.7}$	6.89	5.30 [31]	194.20 [31,57]	20.58 [67]	36.47	14.80
α-$Cu_{50}Zr_{50}$	7.18	3.50 [31]	321.30 [31,57]	3.85 [56]	3.98	14.30
α-$Cu_{33.3}Zr_{66.7}$	6.86	2.80 [31]	384.70 [31,57]	3.68 [a] [68]	3.19	14.80

[a] Calculated using Wiedemann-Franz law $\kappa_e \propto T_e$

B. Samples elaboration

Two crystalline CuZr supercells are prepared using ATOMSK [58], the B_2-$Cu_{50}Zr_{50}$, $C11_b$-$Cu_{33.3}Zr_{66.7}$ of dimension $9.69 \times 3.55 \times 3.55$ nm^3 and $3.56 \times 3.56 \times 12.35$ nm^3 respectively. The energy of the B2 and $C11_b$ are minimized and relaxed using the conjugate gradient algorithm [59]. The system is then replicated along the three directions of space up to a size of about $1092 \times 15 \times 15\ \mathrm{nm}^3$. Periodic boundary conditions (PBCs) are used during the whole preparation process. To cancel residual pressure in the samples during the relaxation, a force norm criterion of 10^{-8} eV/Å is used. Then, the system is thermalized up to 300 K using the NPT ensemble (5 ps) and further equilibrated at constant PT conditions for another 5 ps. To prepare both MGs samples namely α-$Cu_{50}Zr_{50}$ and α-$Cu_{33.3}Zr_{66.7}$, the B_2 and $C11_b$ structures are first equilibrated at 300 K in the NVE ensemble for 100 ps and then heated up to 2000 K above the theoretical melting point $T_m = 1207$ K, 1401 K (±50 K) for $Cu_{50}Zr_{50}$, and $Cu_{33.3}Zr_{66.7}$ respectively using NPT during 170 ps as described in the Supplemental Material [60] (see, also, references [61–65] therein). Annealing is performed at 2000 K for 100 ps to erase the crystalline memory of the samples. This process is followed by a fast quench run from 2000 K to 300 K at a cooling rate of 10^{12} $\mathrm{K\ s^{-1}}$. The obtained glassy states are finally equilibrated at ambient temperature of 300 K for extra 100 ps to remove internal stress within the final structure. The MG are replicated along the 3 directions of space before a last 300 K equilibration run of 10 ps. The damping coefficients of 0.1 ps and 1.0 ps in Nose-Hoover (thermostat-barostat) style are used respectively for temperature and pressure [66]. The MG samples final size is about $874 \times 7 \times 13\ \mathrm{nm}^3$. Finally, for both MGs and crystalline structures the half-part along x of the samples is suppressed (i.e., the matter stands in the $[L_x/2, L_x]$ with L_x the box length along x) to introduce the empty space necessary to accommodate the laser-matter interaction and possible matter ablation.

C. Laser-matter interaction setup

The heat diffusion Eq. (4) is solved numerically on a $702 \times 1 \times 1$ regular electronic cubic mesh as shown in Fig. 1. The laser shot attenuation length are set according to the value shown in Table I. They are computed using the formula described in [31] as $l_p = x l_p^{\mathrm{Cu}} + (1-x) l_p^{\mathrm{Zr}}$, where $l_p^{\mathrm{Cu}} = 12.2$ nm, $l_p^{\mathrm{Zr}} = 16.4$ nm, are penetration depth of Cu, Zr, and x is the percentage of Cu atoms present in each composition. A laser wavelength of 800 nm and a step function $dx \approx 3$ nm for the T_e variation is used. Here, PBCs are set in y and z lateral directions and free boundaries are imposed following the laser shot $x = [100]$. Ultrafast laser irradiation induces a strong temperature gradient normal to the surface, which leads to the generation of a pressure wave (P wave) propagating to the bulk of the target [69,70]. Hence, a trial-and-error approach focused on the gradual extinction of the reflected P wave is used. For this purpose, we define nonreflecting boundary conditions (NRBC), made of a viscous damping region [71–73] with dimensions of $L_{\mathrm{NRBC}} = 100$ nm. A damping factor $\gamma_{\mathrm{damp}} = 2.5\ 10^{-3}$ $\mathrm{eV\,ps\,Å^{-2}}$ is used in this paper in all simulations. The ultrafast process is modeled as a homogeneous dose energy deposition on the surface with a pulse duration of 100 fs. The TTM-MD stage pushes the system to an extreme nonequilibrium state, which is held for 30 ps. The second stage of the simulation is a regular MD run in the NVE ensemble for (i) 170 ps for crystals and (ii) 970 ps for MGs.

III. RESULTS AND DISCUSSION

Here we investigate the influence of a single ultrafast laser pulse on B_2 and $C11_b$ bulk crystalline CuZr as well as on two amorphous phases using atomistic simulations. The pulse duration is 100 fs long and the absorbed fluence is $160\ \mathrm{mJ/cm^2}$. After the energy deposition on the surface, the samples thermalization is achieved by a strong electron − phonon coupling where both electrons and the ions reach the same equilibrium temperature. The final temperature gradient defines the position of the melting front below the surface.

A. Irradiation of $Cu_{50}Zr_{50}$: B_2 crystal and amorphous

Figure 2(a) shows the evolution of the B_2 microstructure during the simulation. The local crystalline structure is investigated by applying the PTM method to the alloyed system without atomic species differentiation, which leads to characterize the B_2 perfect crystal structure and transformed domains environments (liquid, amorphous, or new phase). Just after the laser pulse energy deposition, the upper part of the samples instantaneously melts as shown by the large amount of atoms in defective configurations. At $t = 80$ ps, several voids and bubbles form below the CuZr surface at position $x = 572$ nm and expand rapidly reaching their critical size at $t = 200$ ps. In the mean time, a new crystalline phase nucleates and grows at position $x \sim 700$ nm far deep in the sample starting from $t = 60$ ps as shown in Figs. 2(c) and 2(d).

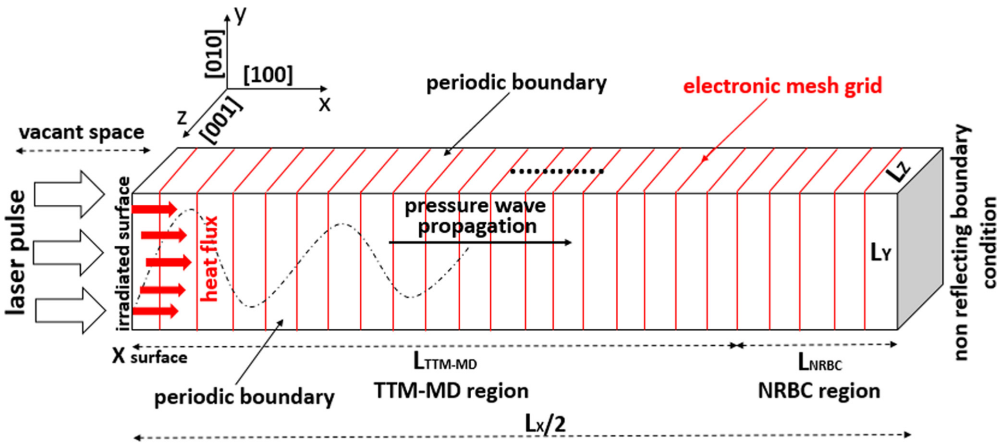

FIG. 1. Simulation setup geometry used to model ultrafast laser pulse interaction in CuZr alloys using TTM-MD simulations. Atoms are located inside the rectangular box and the overlying red grid represents the electronic cell domain for the finite difference solution of Eq. (4). There is no energy transfer with the vacant space beyond the top surface. Additionally, the rear region of the sample represent the NRBC region.

The transformed domain takes the shape of two nanoblades of ∼8.5 nm thickness each that propagate across the sample due to PBCs. The deformation gradient in the x direction displayed in Fig. 2(b) shows that the nanoblades follow a distribution with a spatial pseudoperiodicity separated by a thin B_2 interlayer. A closer look to the transformed structure allows the identification of two simple cubic sublattices attributed to Cu and Zr as in the original B_2 phase. However, the atomic bonding changes from aligned to wavy or *zigzag* configurations along certain directions [see Fig. 2(d)] typical of the B_{19} crystalline structure (e.g., AuCd). This phase transition is similar to the martensitic transformation observed in B_2 NiTi alloys [75–77]. The relative orientation between the two nano-blades allows to confirm the nucleation and propagation of two {111}-oriented B_{19} nanotwins.

The cooperative displacement of atoms requires a significant amount of energy that here relies on the laser pulse. Indeed, the pulse emission is responsible of local temperature gradients, which induce the shock wave (P wave) and then the aforementioned phase transformation. The pressure and temperature profiles time-evolution in the transformed zone are shown in Fig. 3. The pressure profile is characterized by a loading (pressure wave) and unloading (rarefaction wave) P waves. At short times ($t = 0 - 60$ ps), the front of the loading P wave reaches the emphasized region with a maximal value of ∼7 GPa but no transformation is noticed. The B_2 to B_{19} phase transformation that starts at $t = 80$ ps exactly coincides with the appearance of the rarefaction wave (~ -5 GPa extremum) as the loading wave progressively reflects to the colder material. Hence, the phase transition is not due to the

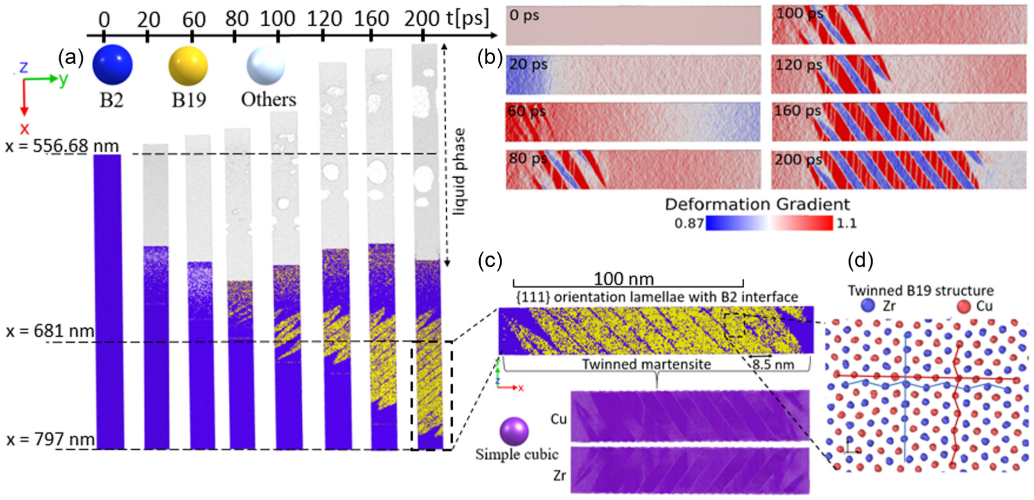

FIG. 2. Snapshots of the atomic configurations evolution in (a) at several times: 0 ps, 20 ps, 60 ps, 80 ps, 100 ps, 120 ps, 160 ps, and 200 ps in B_2-$Cu_{50}Zr_{50}$ target during ultrafast laser irradiation of $\tau = 100$ fs pulse duration and $F_{\mathrm{abs}} = 160\,\mathrm{mJ/cm^2}$ absorbed fluence. The atoms are colored according to their local atomic structure of the binary alloy by using the PTM, the double-dashed arrow in the upper part of target shows the liquefied surface. (b) Deformation gradient in the transformed zone following the x direction at different times computed by the method described in [74]. (c) Zoom on the dashed region where the PTM algorithm is applied on each sublattice monoatomic lattice showing twinned martensite transformation. (d) Enlarged view of the chemical species of the new twinned-B19 phase emergence after the irradiation.

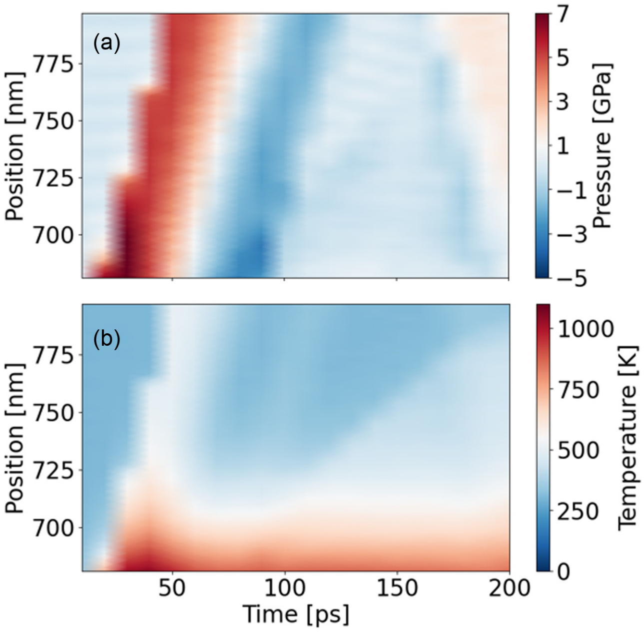

FIG. 3. Spatiotemporal evolution of thermodynamic quantities in the B$_2$-Cu$_{50}$Zr$_{50}$ transformed region located in subsurface (zoom region) area target: (a) pressure and (b) lattice temperature. The initial surface position is given by $x_{\mathrm{surface}} = 556.68$ nm following the x axis direction.

propagation of the pressure wave but more precisely to the unloading one that has exceeded a critical level to activate the transformation [[78]]. Meanwhile, the temperature profile shows an increase up to ~1000 K below the melting temperature $T_m = 1207$ K. A mean T of ~600 K is noticed on the whole transformed zone, confirming that the solid-solid phase transformation observed is driven by mechanical effects as observed in Fig. 2(c). An equivalent protocol was applied to the Cu-Zr amorphous (α-Cu$_{50}$Zr$_{50}$) sample having the same stoichiometry. For comparison purposes with the B$_2$ crystal, identical laser conditions are used while the total simulation time is extended up to 1 ns. Figure 4(a) shows the structural evolution of the α-Cu$_{50}$Zr$_{50}$ sample after the pulse. As in the B$_2$ case, results show surface liquefaction concomitant to the nucleation of voids preceding an ablation event. However, no phase transformation is observed. Regarding the CuZr phase diagram [79], local transformation into B$_2$ is possible and segregation could drive the formation of single crystalline inclusions (with FCC or HCP crystal structure). However, the nucleation of more complex phases is completely excluded. We conclude here that α-Cu$_{50}$Zr$_{50}$ laser-induced local phase transition cannot be obtained using the same laser pulse conditions (duration and fluence) than the one used to phase-transform B$_2$ CuZr crystals.

B. Irradiation of Cu$_{33.3}$Zr$_{66.7}$: C11$_b$ crystal and amorphous

Figure 5 shows the structural evolution of the C11$_b$-Cu$_{33.3}$Zr$_{66.7}$ sample. In particular, it provides the atomistic picture of the point defects generated in this case by the ultrafast pulse. First in the $t = 0 - 100$ ps range, a liquid front is formed characterized by the coalescence of small bubbles formation process that generates voids below the surface in the $t = 100 - 160$ ps range. However, the ablation regime only starts at $t \sim 160$ ps causing a surface expansion of about 60 nm thickness, which expands freely in the vacuum region. Figure 5(b) emphasizes a small area of subsurface material oriented along $x = [100]$. Using this projection, the classical C11$_b$ stacking along $z = [001]$ shows some disturbances and the original [100]-oriented Cu and Zr columns of atoms observed at 0 K can now be schematized by pseudocolumnar domains separated by a thinner layer of atoms attributed to projected elastoplastic deformation (that has not to be confused with sublattice degradation or melting). In addition, point defects are identified up to $x \sim 740$ nm.

Various kinds of point defects including interstitial as well as substitutional Cu and Zr atoms are noticed. Atoms in defective environment (point defects and highly-sheared regions) are identified using a criterion on the atomic displacement along y and z, δy and δz respectively (taking t = 0 as a reference). The displacement criterion is chosen as about half the Cu-Zr or Zr-Zr blond length along y, ensuring to avoid counting atoms fluctuating around their equilibrium position.

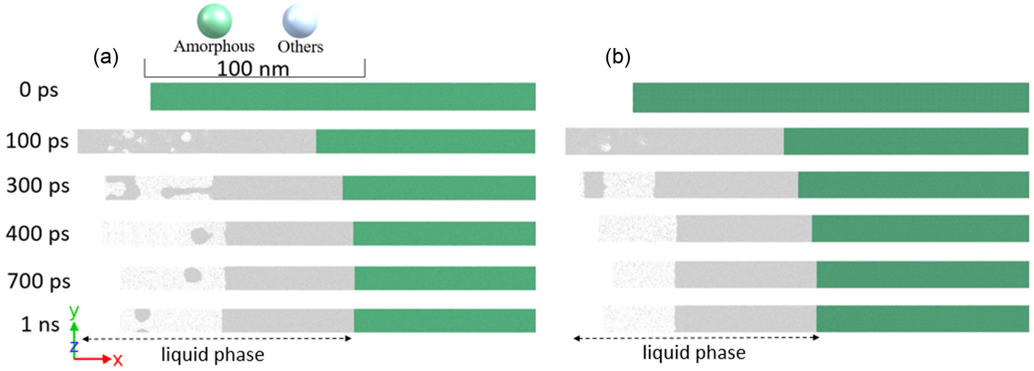

FIG. 4. Snapshots of the structural evolution in the amorphous structures: (a) α-Cu$_{50}$Zr$_{50}$ and (b) α-Cu$_{33.3}$Zr$_{66.7}$ using TTM-MD method at various time steps: 0 ps, 100 ps, 300 ps, 400 ps, 700 ps, and 1 ns. The atoms are colored according to their local atomic structure using PTM algorithm, two atomic contrasts are shown, the zone delimited by a double-dashed arrow in the upper part of targets correspond to liquid phase and the inner part is the amorphous phase. The irradiation conditions are $\tau = 100$ fs pulse duration and $F_{\mathrm{abs}} = 160\,\mathrm{mJ/cm^2}$ of absorbed fluence.

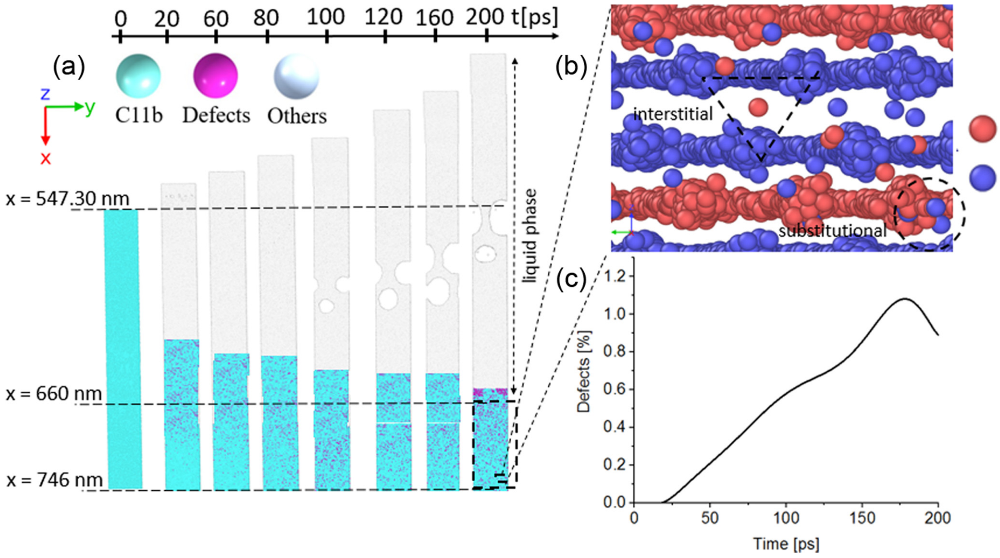

FIG. 5. Snapshots of atomic configurations evolution in (a) at several times: 0 ps, 20 ps, 60 ps, 80 ps, 100 ps, 120 ps, 160 ps, and 200 ps in the $C11_b$-$Cu_{33.3}Zr_{66.7}$ sample target during ultrafast laser irradiation of $\tau = 100$ fs pulse duration and $F_{abs} = 160\,mJ/cm^2$ of absorbed fluence, the double-dashed arrow in the upper part of target shows the liquefied surface. The atoms are colored according to their local atomic structure using PTM algorithm. (b) Enlarged view of interstitial and substitutional defects formation in subsurface within $C11_b$-$Cu_{33.3}Zr_{66.7}$ target after the irradiation at different times. (c) Temporal defects ratio evolution in $Cu_{33.3}Zr_{66.7}$ ($C11_b$) target sorted according to the displacement vector $\delta y > 1$ Å. Atoms satisfying this condition are expected to be in defective positions, this is achieved using displacement vectors analysis [80].

We choose the y and z directions since they are less impacted by the P-wave-induced homogeneous matter displacement merely observed along the x direction. While the amount of atoms with significant δz are only few (0.03% of the atoms in the emphasized zone at $t = 200$ ps), the number of atoms with $\delta y > 1$ Åcontinuously increases during the simulation [Fig. 5(c)]. The anisotropy observed between δy and δz corroborates the observed shear zones in the $z = [001]$ plane. Indeed, no defects are detected in the emphasized domain of the material from $t = 0 - 25$ ps, the fraction of atoms in defective configuration grows up to a maximum 1.12% at $t = 175$ ps before decreasing to 0.93% at the end of the simulation due to relaxation. The defects concentration were computed by evaluating $N_{defects}/N_{total}$ in the total system volume region (241 984 nm^3), where $N_{defects}$ (69 985 atoms) and N_{total} (6 248 652 atoms) are the number of defects and the number of atoms, respectively.

To better understand this phenomenon, we again look at the PT profiles as shown in Fig. 6. Figure 6(a) shows that a strong P wave is generated and reaches a maximum value of ∼8 GPa at $t = 20$ ps. At $t = 60$ ps the rarefaction P wave propagates with a negative extremum front of ~ -6 GPa appears. The rarefaction wave and the defects population are highly correlated in terms of space and time. The lattice temperature shown in Fig. 6(b) confirms that at the liquid-solid interface the temperature is ∼2000 K, higher than the melting point $T_m = 1401$ K. We have to mention that below the solid-liquid interface the system is highly perturbed due to heat diffusion phenomenon but not melted. Here we show that the electron − phonon coupling plays an important role in the laser-matter interaction, and since the coupling factor is stronger for $C11_b$-$Cu_{33.3}Zr_{66.7}$ than for B_2-$Cu_{50}Zr_{50}$ (cf. Table I) the temperature and P-wave maximum are higher in the case of $C11_b$-$Cu_{33.3}Zr_{66.7}$.

Finally, the amorphous α-$Cu_{33.3}Zr_{66.7}$ sample is subjected to a 1-ns simulation with same fluence and pulse duration. Results are shown in Fig. 4(b). A spallation process is noticed

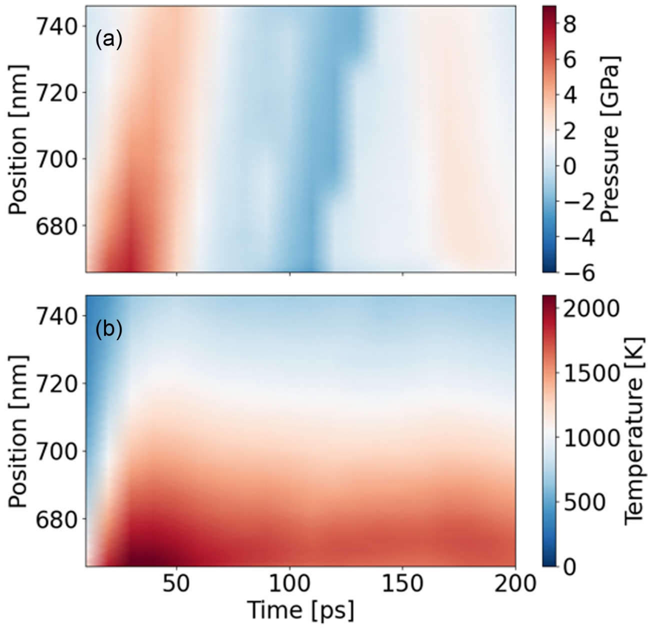

FIG. 6. Spatiotemporal evolution of thermodynamic quantities in the subsurface transformed region (zoom region): (a) pressure and (b) lattice temperature evolution in $C11_b$-$Cu_{33.3}Zr_{66.7}$ sample target. The initial surface position is given by $x_{surface} = 547.30$ nm following the x axis direction.

at t = 100 ps through the growth of subsurface voids inducing the ejection of a top liquid layer but again without any sign of crystal nucleation. One can hypothesize that the absence of crystallization is due to (i) the tensile rarefaction wave magnitude sufficient enough to induce spallation in the molten part but not to reorganize atoms in an ordered manner or (ii) a nonfavorable stoichiometry.

IV. CONCLUSIONS

The local subsurface structural phase transition and defects formation process attributed to ultrafast laser shot in crystalline CuZr systems are predicted using TTM-MD atomistic calculations. In summary, using the same laser conditions, two remarkable outcomes are reported here depending on the initial crystallographic structures. The original B_2 crystalline sample phase transform into twinned B_{19} while $C11_b$ shows a huge deformation pattern including points defects and shear zones. Both transformations are driven by the rarefaction pressure wave. They are permanent as the materials reach metastable states in our calculations and localized within the subsurface. Therefore, they can be captured experimentally. Concerning the B_2 structure, the simulation corroborates that the phase transformation and the twinning process emerges in a quasi-ordered manner, exhibiting no spatial variability across the crystalline structure. In contrast, the response of the $C11_b$ structure is different as the defects generation is noticed instead of a martensite phase transition. On the other hand, the response of the irradiated MGs counterparts show a completely different structural response. Indeed, no crystallization is noticed for the same laser conditions. Besides the surface ablation in the MGs, we might have expected the laser shock to induce recrystallization by playing a similar role as a nanoindenter [81–83].

Targeting innovative technological applications requires the control of local crystalline structures properties at the nanoscale that can be promoted by laser-matter interactions. Dislocations and twins that appear at the nanoscale as a strain relaxation mechanism can be frozen within a solid alloy. As predicted in the B_2 structure, this leads to the emergence of advantageous mechanical properties [84]. Nano-sized twins are known to enhance hardness [85] and nano-twinned materials become more resilient to fracture and fatigue crack initiation during plastic deformation [86]. Nano-architecturing of the $C11_b$ structure with defects (points defects, dislocations, stacking faults) could be exploited for battery applications [87], elaboration of high-performance thermoelectric materials [88], or improving the fracture toughness [89]. The originality of this paper is that ultrafast laser irradiation could provide an effective method to tune a new generation of nano-architectured CuZr alloys, which might open new routes for future industrial applications.

ACKNOWLEDGMENTS

This work is supported by the ANR Project MEGALIT (No. ANR-18-CE08) and the Project FORMEL of the Pack Ambition Research program of the Auvergne Rhône-Alpes Region. Numerical calculations have been performed using HPC resources from GENCI-TGCC, CINES (Project gen7041) and P2HPD computing center facility of Lyon university.

---

[1] E. G. Gamaly, The physics of ultra-short laser interaction with solids at non-relativistic intensities, Phys. Rep. **508**, 91 (2011).

[2] R. Stoian and J.-P. Colombier, Advances in ultrafast laser structuring of materials at the nanoscale, Nanophotonics **9**, 4665 (2020).

[3] T. Danz, T. Domröse, and C. Ropers, Ultrafast nanoimaging of the order parameter in a structural phase transition, Science **371**, 371 (2021).

[4] J. Takeda, W. Oba, Y. Minami, T. Saiki, and I. Katayama, Ultrafast crystalline-to-amorphous phase transition in $Ge_2Sb_2Te_5$ chalcogenide alloy thin film using single-shot imaging spectroscopy, Appl. Phys. Lett. **104**, 261903 (2014).

[5] R. Buividas, G. Gervinskas, A. Tadich, B. C. Cowie, V. Mizeikis, A. Vailionis, D. de Ligny, E. G. Gamaly, A. V. Rode, and S. Juodkazis, Phase transformation in laser-induced micro-explosion in olivine $(Fe,Mg)_2SiO_4$, Adv. Eng. Mater. **16**, 767 (2014).

[6] L. Bressel, D. de Ligny, C. Sonneville, V. Martinez, V. Mizeikis, Buividas, and S. Juodkazis, Femtosecond laser induced density changes in GeO_2 and SiO_2 glasses: Fictive temperature effect, Opt. Mater. Express **1**, 605 (2011).

[7] K. Sokolowski-Tinten, J. Bialkowski, M. Boing, A. Cavalleri, and D. von der Linde, Thermal and nonthermal melting of gallium arsenide after femtosecond laser excitation, Phys. Rev. B **58**, R11805 (1998).

[8] S. Sundaram and E. Mazur, Inducing and probing non-thermal transitions in semiconductors using femtosecond laser pulses, Nat. Mater. **1**, 217 (2002).

[9] A. Cavalleri, C. Tóth, C. W. Siders, J. A. Squier, F. Ráksi, P. Forget, and J. C. Kieffer, Femtosecond Structural Dynamics in VO_2 during an Ultrafast Solid-Solid Phase Transition, Phys. Rev. Lett. **87**, 237401 (2001).

[10] S. Wall, D. Wegkamp, L. Foglia, K. Appavoo, J. Nag, R. Haglund, J. Stähler, and M. Wolf, Ultrafast changes in lattice symmetry probed by coherent phonons, Nat. Commun. **3**, 721 (2012).

[11] H. Urbassek and L. Sandoval, Molecular dynamics modeling of martensitic transformations in steels, Phase transformations in steels, 433 (2012).

[12] C.-H. Lu, E. Hahn, B. Remington, B. Maddox, E. Bringa, and M. Meyers, Phase transformation in tantalum under extreme laser deformation, Sci. Rep. **5**, 15064 (2015).

[13] W. Petry, A. Heiming, J. Trampenau, M. Alba, C. Herzig, H. R. Schober, and G. Vogl, Phonon dispersion of the bcc phase of group-IV metals. I. bcc titanium, Phys. Rev. B **43**, 10933 (1991).

[14] J. H. Li and B. X. Liu, Structural phase transformation in Ni–Hf and Ni–Ti systems studied by molecular dynamics simulation, J. Phys. Soc. Jpn. **74**, 2699 (2005).

[15] Y. R. Kolobov, E. Golosov, T. Vershinina, M. Zhidkov, A. Ionin, S. Kudryashov, S. Makarov, L. Seleznev, D. Sinitsyn, and A. Ligachev, Structural transformation and residual stresses in surface layers of $\alpha + \beta$ titanium alloys nanotextured by femtosecond laser pulses, Appl. Phys. A **119**, 241 (2015).

[16] S. T. Murphy, S. L. Daraszewicz, Y. Giret, M. Watkins, A. L. Shluger, K. Tanimura, and D. M. Duffy, Dynamical simulations of an electronically induced solid-solid phase transformation in tungsten, Phys. Rev. B **92**, 134110 (2015).

[17] L. Ben-Mahfoud, E. P. Silaeva, R. Stoian, and J. P. Colombier, Structural instability of transition metals upon ultrafast laser irradiation, Phys. Rev. B **104**, 104104 (2021).

[18] G. Kumar, H. X. Tang, and J. Schroers, Nanomoulding with amorphous metals, Nature (London) **457**, 868 (2009).

[19] S. I. Anisimov, Electron emission from metal surfaces exposed to ultrashort laser pulses, Sov. Phys. JETP **39**, 3 (1975).

[20] D. M. Duffy and A. M. Rutherford, Including the effects of electronic stopping and electron–ion interactions in radiation damage simulations, J. Phys.: Condens. Matter **19**, 016207 (2007).

[21] A. M. Rutherford and D. M. Duffy, The effect of electron–ion interactions on radiation damage simulations, J. Phys.: Condens. Matter **19**, 496201 (2007).

[22] Z. Lin, R. A. Johnson, and L. V. Zhigilei, Computational study of the generation of crystal defects in a bcc metal target irradiated by short laser pulses, Phys. Rev. B **77**, 214108 (2008).

[23] X. Sedao, M. V. Shugaev, C. Wu, T. Douillard, C. Esnouf, C. Maurice, S. Reynaud, F. Pigeon, F. Garrelie, L. V. Zhigilei, *et al.*, Growth twinning and generation of high-frequency surface nanostructures in ultrafast laser-induced transient melting and resolidification, ACS Nano **10**, 6995 (2016).

[24] D. S. Ivanov and L. V. Zhigilei, Combined atomistic-continuum modeling of short-pulse laser melting and disintegration of metal films, Phys. Rev. B **68**, 064114 (2003).

[25] C. Wu and L. V. Zhigilei, Microscopic mechanisms of laser spallation and ablation of metal targets from large-scale molecular dynamics simulations, Appl. Phys. A **114**, 11 (2014).

[26] E. T. Karim, Z. Lin, and L. V. Zhigilei, Molecular dynamics study of femtosecond laser interactions with Cr targets, AIP Conf. Proc. **1464**, 280 (2012).

[27] M. R. Karim, M. Kattoura, S. R. Mannava, V. K. Vasudevan, A. S. Malik, and D. Qian, A computational study on the microstructural evolution in near-surface copper grain boundary structures due to femtosecond laser processing, Comp. Mech. **61**, 105 (2018).

[28] V. Stegailov, S. Starikov, and G. Norman, Atomistic simulation of laser ablation of gold: The effect of electronic pressure, AIP Conf. Proc. **1426**, 905 (2012).

[29] B. S. Lee and S. Park, Applying tersoff-potential and bond-softening models in a molecular dynamics study of femtosecond laser processing, J. Appl. Phys. **126**, 045109 (2019).

[30] H. O. Jeschke, M. E. Garcia, and K. H. Bennemann, Theory for the Ultrafast Ablation of Graphite Films, Phys. Rev. Lett. **87**, 015003 (2001).

[31] S. Marinier and L. J. Lewis, Femtosecond laser ablation of Cu_xZr_{1-x} bulk metallic glasses: A molecular dynamics study, Phys. Rev. B **92**, 184108 (2015).

[32] H.-W. Chen, K.-C. Hsu, Y.-C. Chan, J.-G. Duh, J.-W. Lee, J. S.-C. Jang, and G.-J. Chen, Antimicrobial properties of Zr–Cu–Al–Ag thin film metallic glass, Thin Solid Films **561**, 98 (2014).

[33] L. Yu, J. Tang, H. Wang, Y. Wang, J. Qiao, M. Apreutesei, and B. Normand, Corrosion behavior of bulk $(Zr_{58}Nb_3Cu_{16}Ni_{13}Al_{10})_{100-x}Y_x$ (X= 0, 0.5, 2.5 at.%) metallic glasses in sulfuric acid, Corr. Sci. **150**, 42 (2019).

[34] C. Li, H. Zhang, G. Cheng, N. Faure, D. Jamon, J.-P. Colombier, and R. Stoian, Initial cumulative effects in femtosecond pulsed laser-induced periodic surface structures on bulk metallic glasses, J. Laser Micro Nanoeng. **11**, 357 (2016).

[35] M. Prudent, F. Bourquard, A. Borroto, J.-F. Pierson, F. Garrelie, and J.-P. Colombier, Initial morphology and feedback effects on laser-induced periodic nanostructuring of thin-film metallic glasses, Nanomaterials **11**, 1076 (2021).

[36] M. S. Titus, M. P. Echlin, P. Gumbsch, and T. M. Pollock, Dislocation injection in strontium titanate by femtosecond laser pulses, J. Appl. Phys. **118**, 075901 (2015).

[37] M. P. Echlin, M. S. Titus, M. Straw, P. Gumbsch, and T. M. Pollock, Materials response to glancing incidence femtosecond laser ablation, Acta Mater. **124**, 37 (2017).

[38] M. He, C. Wu, M. V. Shugaev, G. D. Samolyuk, and L. V. Zhigilei, Computational study of short-pulse laser-induced generation of crystal defects in Ni-based single-phase binary solid–solution alloys, J. Phys. Chem. C **123**, 2202 (2019).

[39] D. S. Ivanov, Z. Lin, B. Rethfeld, G. M. O'Connor, T. J. Glynn, and L. V. Zhigilei, Nanocrystalline structure of nanobump generated by localized photoexcitation of metal film, J. Appl. Phys. **107**, 013519 (2010).

[40] C. Wu, M. S. Christensen, J.-M. Savolainen, P. Balling, and L. V. Zhigilei, Generation of subsurface voids and a nanocrystalline surface layer in femtosecond laser irradiation of a single-crystal Ag target, Phys. Rev. B **91**, 035413 (2015).

[41] S. Zhou and R. Napolitano, Phase stability for the Cu–Zr system: First-principles, experiments and solution-based modeling, Acta Mater. **58**, 2186 (2010).

[42] S. Plimpton, Fast parallel algorithms for short-range molecular dynamics, J. Comput. Phys. **117**, 1 (1995).

[43] M. Mendelev, Y. Sun, F. Zhang, C.-Z. Wang, and K.-M. Ho, Development of a semi-empirical potential suitable for molecular dynamics simulation of vitrification in Cu-Zr alloys, J. Chem. Phys. **151**, 214502 (2019).

[44] P. M. Larsen, S. Schmidt, and J. Schiøtz, Robust structural identification via polyhedral template matching, Modell. Simul. Mater. Sci. Eng. **24**, 055007 (2016).

[45] A. Stukowski, Visualization and analysis of atomistic simulation data with ovito-the open visualization tool, Modell. Simul. Mater. Sci. Eng. **18**, 015012 (2010).

[46] https://lammps.sandia.gov/doc/fix_ttm.html.

[47] A. Jay, M. Raine, N. Richard, N. Mousseau, V. Goiffon, A. Hémeryck, and P. Magnan, Simulation of single particle displacement damage in silicon-Part II: Generation and long-time relaxation of damage structure, IEEE Trans. Nucl. Sci. **64**, 141 (2017).

[48] J. Chen, D. Tzou, and J. Beraun, A semiclassical two-temperature model for ultrafast laser heating, Int. J. Heat Mass Transf. **49**, 307 (2006).

[49] G. Norman, S. Starikov, V. Stegailov, I. Saitov, and P. Zhilyaev, Atomistic modeling of warm dense matter in the two-temperature state, Contrib. Plasma Phys. **53**, 129 (2013).

[50] V. Pisarev and S. Starikov, Atomistic simulation of ion track formation in UO_2, J. Phys.: Condens. Matter **26**, 475401 (2014).

[51] M. A. Seaton, I. T. Todorov, S. L. Daraszewicz, G. S. Khara, and D. M. Duffy, Domain decomposition of the two-temperature model in DL_POLY_4, Mol. Simul. **47**, 180 (2021).

[52] S. L. Daraszewicz, Y. Giret, H. Tanimura, D. M. Duffy, A. L. Shluger, and K. Tanimura, Determination of the electron–phonon coupling constant in tungsten, Appl. Phys. Lett. **105**, 023112 (2014).

[53] C. L. Phillips, R. J. Magyar, and P. S. Crozier, A two-temperature model of radiation damage in α-quartz, J. Chem. Phys. **133**, 144711 (2010).

[54] Z. D. McClure, S. T. Reeve, and A. Strachan, Role of electronic thermal transport in amorphous metal recrystallization: A molecular dynamics study, J. Chem. Phys. **149**, 064502 (2018).

[55] C. Kittel, *Introduction to Solid State Physics* (Wiley, Hoboken, NJ, 2004).

[56] C. L. Choy, K. W. Tong, H. K. Wong, and W. P. Leung, Thermal conductivity of amorphous alloys above room temperature, J. Appl. Phys. **70**, 4919 (1991).

[57] P. Garoche and J. Bigot, Comparison between amorphous and crystalline phases of copper-zirconium alloys by specific-heat measurements, Phys. Rev. B **28**, 6886 (1983).

[58] P. Hirel, Atomsk: A tool for manipulating and converting atomic data files, Comput. Phys. Commun. **197**, 212 (2015).

[59] G. Yuan, Z. Wei, and Q. Zhao, A modified Polak-Ribière-Polyak conjugate gradient algorithm for large-scale optimization problems, IIE Transactions **46**, 397 (2014).

[60] See Supplemental Material at http://link.aps.org/supplemental/10.1103/PhysRevMaterials.6.126001 for computational details about structural properties of crystalline and amorphous CuZr alloys.

[61] A. Kokalj, Xcrysden-a new program for displaying crystalline structures and electron densities, J. Mol. Graphics Modell. **17**, 176 (1999).

[62] D. A. Porter and K. E. Easterling, *Phase Transformations in Metals and Alloys (revised reprint)* (CRC Press, Boca Raton, FL, 2009).

[63] W. Zhang, Y. Peng, and Z. Liu, Molecular dynamics simulations of the melting curve of NiAl alloy under pressure, AIP Adv. **4**, 057110 (2014).

[64] X. Gonze, B. Amadon, G. Antonius, F. Arnardi, L. Baguet, J.-M. Beuken, J. Bieder, F. Bottin, J. Bouchet, E. Bousquet *et al.*, The ABINIT project: Impact, environment and recent developments, Comput. Phys. Commun. **248**, 107042 (2020).

[65] M. Torrent, F. Jollet, F. Bottin, G. Zérah, and X. Gonze, Implementation of the projector augmented-wave method in the ABINIT code: Application to the study of iron under pressure, Comput. Mater. Sci. **42**, 337 (2008).

[66] D. J. Evans and B. L. Holian, The nose–hoover thermostat, J. Chem. Phys. **83**, 4069 (1985).

[67] S. Uporov, V. Bykov, and S. Estemirova, Electrical and thermal conductivities of rapidly crystallized Cu-Zr alloys: The effect of anharmonicity, Phys. B: Condens. Matter **499**, 97 (2016).

[68] G. Firstov, A. Timoshevskii, Y. N. Koval, S. Kalkuta, and J. Van Humbeeck, Phase stability during martensitic transformation in ZrCu intermetallics: crystal and electronic structure aspects, in *European Symposium on Martensitic Transformations*, Proceeding of ESOMAT (EDP Sciences, 2009) p. 02008.

[69] M. V. Shugaev and L. V. Zhigilei, Thermoelastic modeling of laser-induced generation of strong surface acoustic waves, J. Appl. Phys. **130**, 185108 (2021).

[70] M. V. Shugaev, M. He, Y. Levy, A. Mazzi, A. Miotello, N. M. Bulgakova, and L. V. Zhigilei, Laser-induced thermal processes: Heat transfer, generation of stresses, melting and solidification, vaporization, and phase explosion, in *Handbook of Laser Micro- and Nano-Engineering*, edited by K. Sugioka (Springer International Publishing, Cham, 2020) pp. 1–81.

[71] https://docs.lammps.org/fix_viscous.html.

[72] C. Schäfer, H. M. Urbassek, and L. V. Zhigilei, Metal ablation by picosecond laser pulses: A hybrid simulation, Phys. Rev. B **66**, 115404 (2002).

[73] L. V. Zhigilei, Z. Lin, and D. S. Ivanov, Atomistic modeling of short pulse laser ablation of metals: Connections between melting, spallation, and phase explosion, J. Phys. Chem. C **113**, 11892 (2009).

[74] A. Stukowski and A. Arsenlis, On the elastic–plastic decomposition of crystal deformation at the atomic scale, Modell. Simul. Mater. Sci. Eng. **20**, 035012 (2012).

[75] X. Zhang and H. Sehitoglu, Crystallography of the B2 → R → B19′ phase transformations in NiTi, Mater. Sci. Eng. A **374**, 292 (2004).

[76] W.-S. Ko, B. Grabowski, and J. Neugebauer, Development and application of a Ni-Ti interatomic potential with high predictive accuracy of the martensitic phase transition, Phys. Rev. B **92**, 134107 (2015).

[77] J. Bowles and J. Mackenzie, The crystallography of martensite transformationsi, Acta Metall. **2**, 129 (1954).

[78] V. K. Sutrakar and D. R. Mahapatra, Single and multi-step phase transformation in CuZr nanowire under compressive/tensile loading, Intermetallics **18**, 679 (2010).

[79] D. Arias and J. Abriata, Cu-Zr (copper-zirconium), J. Phase Equilib. **11**, 452 (1990).

[80] https://www.ovito.org/docs/current/reference/pipelines/modifiers/displacement_vectors.html.

[81] J. Sort, L. F. Bonavina, A. Varea, C. Souza, W. J. Botta, C. S. Kiminami, C. Bolfarini, S. Surinach, M. D. Baró, and J. Nogués, Out-of-plane magnetic patterning based on indentation-induced nanocrystallization of a metallic glass, Small **6**, 1543 (2010).

[82] J. Fornell, E. Rossinyol, S. Surinach, M. Baró, W. Li, and J. Sort, Enhanced mechanical properties in a Zr-based metallic glass caused by deformation-induced nanocrystallization, Scr. Mater. **62**, 13 (2010).

[83] Z. Ma, F. Lu, X. Ma, H. Zhao, K. Zeng, and L. Ren, Cyclic stress induced surface nanocrystallization adjacent to indentation edge of Zr-based bulk metallic glass at room temperature, Appl. Surf. Sci. **506**, 145044 (2020).

[84] Z. Zhang, H. Sheng, Z. Wang, B. Gludovatz, Z. Zhang, E. P. George, Q. Yu, S. X. Mao, and R. O. Ritchie, Dislocation mechanisms and 3D twin architectures generate exceptional strength-ductility-toughness combination in CrCoNi medium-entropy alloy, Nat. Commun. **8**, 14390 (2017).

[85] Y. Tian, B. Xu, D. Yu, Y. Ma, Y. Wang, Y. Jiang, W. Hu, C. Tang, Y. Gao, K. Luo *et al.*, Ultrahard nanotwinned cubic boron nitride, Nature (London) **493**, 385 (2013).

[86] P. Uttam, V. Kumar, K.-H. Kim, and A. Deep, Nanotwinning: Generation, properties, and application, Mater. Des. **192**, 108752 (2020).

[87] Y. Pan, Y. Li, Q. Zheng, and Y. Xu, Point defect of titanium sesquioxide Ti_2O_3 as the application of next generation li-ion batteries, J. Alloys Compd. **786**, 621 (2019).

[88] L. Hu, T. Zhu, X. Liu, and X. Zhao, Point defect engineering of high-performance bismuth-telluride-based thermoelectric materials, Adv. Funct. Mater. **24**, 5211 (2014).

[89] C. Liu, J. Zhu, M. Brady, C. McKamey, and L. Pike, Physical metallurgy and mechanical properties of transition-metal laves phase alloys, Intermetallics **8**, 1119 (2000).